ChemComm



COMMUNICATION

View Article Online



Cite this: Chem. Commun., 2025. **61**, 11826

Received 1st June 2025, Accepted 30th June 2025

DOI: 10.1039/d5cc03109e

rsc.li/chemcomm

Nano-silicon/reduced graphene oxide composite anodes for high performance all solid-state batteries*

Ayush Morchhale, ‡a Dawoon Jang, ‡a Jun Wei Yap, Lakshmi Surag Singavarapu, b Sadikul Alam, b Jinwoo Hwang, b Sungjin Park b and Jung-Hyun Kim b *a

Nano-Si (n-Si) encapsulated with SiO_x shells and anchored onto reduced graphene oxide (rGO) via hydrothermal self-assembly is demonstrated as a promising solid-state battery anode. Compared to simple n-Si, this composite anode exhibited improved rate capability and cycle life, enabled by robust Si-O-C bonding, mechanical reinforcement, and rapid electron transport.

Sulfide-based all solid-state batteries (SSBs) have emerged as prominent next-generation energy storage devices due to their potential for enhanced safety and energy density compared to conventional lithium-ion batteries. 1,2 Despite significant progress, sulfide-based SSBs still face critical challenges at the anode/solid electrolyte (SE) interface, especially when using Si anodes.³ While Si offers high theoretical capacity (4200 mAh g⁻¹ for Li_{4.4}Si) compared to traditional graphite anodes (372 mAh g⁻¹), its practical application has been hindered by electro-chemomechanical instabilities.4 Large volume expansions (>300%) of the Si anode during cycling induce severe mechanical stresses at the anode/SE interface, leading to rapid capacity fading, SE cracking, and premature cell failure.5 Resolving this interfacial instability is critical, as the adoption of Si anodes for SSBs enables substantial improvements in energy density, driving range, fastthe widespread adoption of electric vehicles (EVs).

nanoscale interfaces, a limited understanding of the underlying degradation mechanisms, and the lack of effective in situ

characterization tools.⁶ The most common approach has been replacing micron-sized Si particles with nano-sized Si (n-Si) particles, which can alleviate stress accumulation and mitigate subsequent mechanical degradation.7 However, the current approach to stabilize n-Si in sulfide-based SSBs remains insufficient. A major issue lies in the intrinsically low electronic conductivity and limited Li⁺ diffusivity of n-Si based anodes, which further exacerbate their electro-chemo-mechanical instability.

To solve the Si/SE interfacial problems, we introduced n-Si particles coated with a conformal SiO_x shell, which are chemically anchored onto reduced graphene oxide (rGO) nanoplatelets. While the enhanced performance of this chemically modified anode (hereafter referred to as n-Si/G) has been demonstrated in Li-ion batteries, 8-10 its impact in sulfide-based SSBs has vet to be fully explored. In this work, n-Si/G powder samples were prepared via one-pot hydrothermal reaction. The SiO_x shell offers moderate Liion conductivity ($\sim 1 \mu \text{S cm}^{-1}$)¹¹ due to its amorphous structure and serves as a chemically and mechanically stable interfacial layer that mitigates direct contact between the Si core and the argyroditetype Li₆PS₅Cl_{0.5}Br_{0.5} SE. ^{10,12} The covalent Si-O-C bonding between the Si@SiOx nanoparticles and rGO nanoplatelets ensures strong interfacial adhesion, enhancing structural integrity and effectively accommodating volumetric changes during cycling. 13

Fig. 1a displays the uniform dispersion of n-Si particles onto the rGO supports, as observed by scanning electron microscopy (SEM). Its transmission electron microscopy (TEM) image (Fig. 1b) reveals an \sim 3 nm thick SiO_x shell surrounding the n-Si particles. Highangle annular dark field scanning transmission electron microscopy (HAADF-STEM) images (Fig. 1c and 1d) reveal n-Si particles, with diameters ranging from 30 to 50 nm, anchored on the rGO layers. Fig. 1c and e-g show energy-dispersive X-ray spectroscopy (EDS) mapping images displaying the elemental distribution of Si, C, and O on the surface of the n-Si/G particles. The SiO_x nanoparticles are uniformly distributed on the rGO layers.

X-ray photoelectron spectroscopy (XPS) was performed to analyze the chemical states of the n-Si/G composite. As shown in Fig. 1h, the deconvoluted C 1s spectrum of the n-Si/G

charging capability, and overall safety, which are key factors for Addressing the electro-chemo-mechanical instability of Si in SSBs remains challenging due to the complex interactions at the

^a Department of Mechanical and Aerospace Engineering, The Ohio State University, Columbus, Ohio 43210, USA. E-mail: kim.6776@osu.edu

^b Department of Materials Science and Engineering, The Ohio State University, Columbus, Ohio 43210, USA

^c Department of Chemistry and Chemical Engineering, Inha University, 100 Inha-ro, Michuhol-gu, Incheon 22212, Republic of Korea

[†] Electronic supplementary information (ESI) available. See DOI: https://doi.org/ 10.1039/d5cc03109e

[‡] These authors contributed equally.

Communication

C Si O C C=C/C-C-O-Si C-OH C-O C=O COOH rGO Intensity (A.U.) Fitting 50 nm 290 288 282 Si⁰ 2p_{3/2} **Fitting** Si⁰ 2p_{1/2} Si-O-C

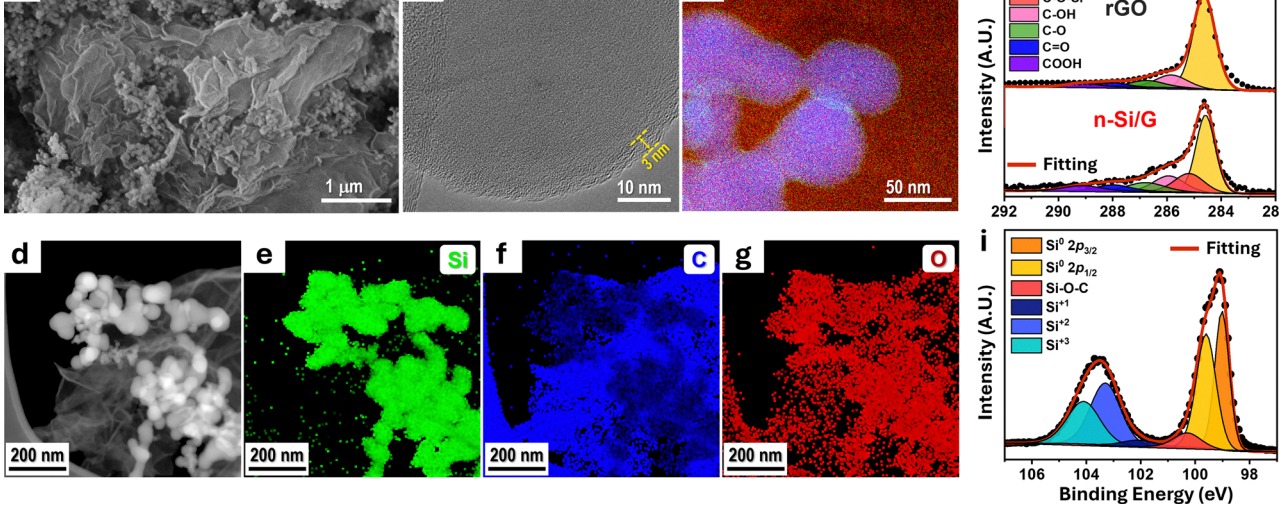


Fig. 1 (a) SEM, (b) TEM, and (c)-(g) STEM-EDS images of the n-Si/G samples. The TEM image focused on a single n-Si particle within the n-Si/G. (h) C 1s XPS spectra of the rGO and n-Si/G sample. (i) Si 2p XPS spectra of the n-Si/G sample (circular dots: experimental data, solid lines: fitting curves).

composite exhibits six peaks at 284.6, 285.2, 285.9, 286.7, 288.0 and 289.1 eV, corresponding to C=C/C-C, C-O-Si, C-OH, C-O, C=O, and COOH bonds, respectively (Fig. 1h). The peak at 285.2 eV is attributed to the new formation of Si-O-C bonds arising from the chemical bonding between the SiO_x and rGO layers. Meanwhile, the intensity of the C=C/C-C peak, originating from the rGO, decreased as a result of bonding with SiO_x in the n-Si/G sample. In the deconvoluted Si 2p spectrum of the n-Si/G composite (Fig. 1i), distinct peaks were observed corresponding to metallic silicon: Si $2p_{3/2}$ at 99.0 eV and Si $2p_{1/2}$ at 99.6 eV. In addition, a peak at 100.3 eV is attributed to Si-O-C bonding, whereas peaks at 102.0, 103.3, and 104.0 eV correspond to oxidized Si species with oxidation states of Si⁺¹, Si⁺², and Si⁺³, respectively, further confirming the presence of the SiO_x outer shell. This result is consistent with the TEM data (Fig. 1b and c), which showed SiO_x shells surrounding the n-Si particles, while metallic Si remains predominantly confined to the particle cores.

The electrochemical performance of the n-Si/G anodes was evaluated using SSB full-cells. For cathodes, single-crystal LiNi_{0.6}Mn_{0.2}Co_{0.2}O₂ (NMC622) was coated with 1 wt% LiNbO₃ (LNO) to passivate the cathode/SE interface. In this work, all the SSB cells were cycled under a constant stack pressure of 5 MPa. Fig. 2a presents the long-term cycle life of SSB full-cells at room temperature (RT). The full cell with the n-Si/G anode delivered an initial discharge capacity of 169 mAh g^{-1} at C/10, with a 1st cycle coulombic efficiency (CE) of 75%, compared to 172 mAh g⁻¹ and 71% for the full cell with the simple n-Si anode. Between the 4th and 50th cycles at C/5, the n-Si/G anode offered improved capacity retention (93%) relative to the n-Si anode (87%). Fig. 2b and c shows the voltage profiles of the fullcells at the 1st, 5th, and 50th cycles. The simple n-Si anode showed larger voltage drops $(\Delta V = I \cdot \Delta R)$ with cycle number, indicating greater cell-resistance growth (ΔR) compared to the n-Si/G anode. This could be due to the possible microstructural degradation of the n-Si anodes.

The impact of n-Si/G anodes on the rate capability of SSB full-cells was examined across various C-rates ranging from C/ 10 to 1C at RT (Fig. 2d). The full-cell with the simple n-Si anode had 169 mAh g^{-1} at C/10 (5th cycle), 144 mAh g^{-1} at C/5 (10th cycle), 122 mAh g^{-1} at C/3 (15th cycle), 99 mAh g^{-1} at C/2 (20th cycle), 67 mAh g^{-1} at 1C (25th cycle), and 151 mAh g^{-1} at C/10 (30th cycle). The cell exhibited an overall capacity retention of 86% at C/10 after 30 accelerated rate tests. In contrast, the full cell with the n-Si/G anode exhibited significantly improved rate capability, achieving an overall capacity retention of 96% at C/ 10 after 30 accelerated rate tests. For example, it delivered 165 mAh g^{-1} at C/10 (5th cycle), 149 mAh g^{-1} at C/5 (10th cycle), 132 mAh g^{-1} at C/3 (15th cycle), 116 mAh g^{-1} at C/2 (20th cycle), 97 mAh g^{-1} at 1C (25th cycle), and 161 mAh g^{-1} at C/10 (30th cycle). The n-Si/G anode exhibited a 44.8% increase in capacity at 1C charging compared to the n-Si anode.

To elucidate the superior rate capability and capacity retention of the n-Si/G anode relative to the simple n-Si anode, electrochemical impedance spectroscopy (EIS) combined with distribution of relaxation times (DRT) analysis was performed on the fullcells. Fig. 3a shows the Nyquist plots of SSB full-cells with simple n-Si and n-Si/G anodes, measured at 50% state-of-charge (SOC) and RT over a frequency range of 5 MHz and 50 mHz. Fig. 3b and c illustrate their corresponding DRT profiles for each cell. The resulting Nyquist plots were further processed via the distribution of relaxation time (DRT) technique MATLAB code developed by Wan et al. 14 All subsequent analyses derived from the Nyquist and DRT plots were based on interpretations established in prior studies of SSBs. 15-17 The high frequency intercept (f > 3 MHz) in the Nyquist plot corresponds to the bulk resistance (R_B) of the SE. The first semi-circle, corresponding to the P1 peak in the DRT profile at ~ 0.5 MHz is attributed to the grain boundary resistance $(R_{\rm GB})$. The second large semi-circles (between 200 kHz and 1 Hz) in the Nyquist plots were deconvoluted using DRT into contributions from chemical contact resistance (RC) for P2, and

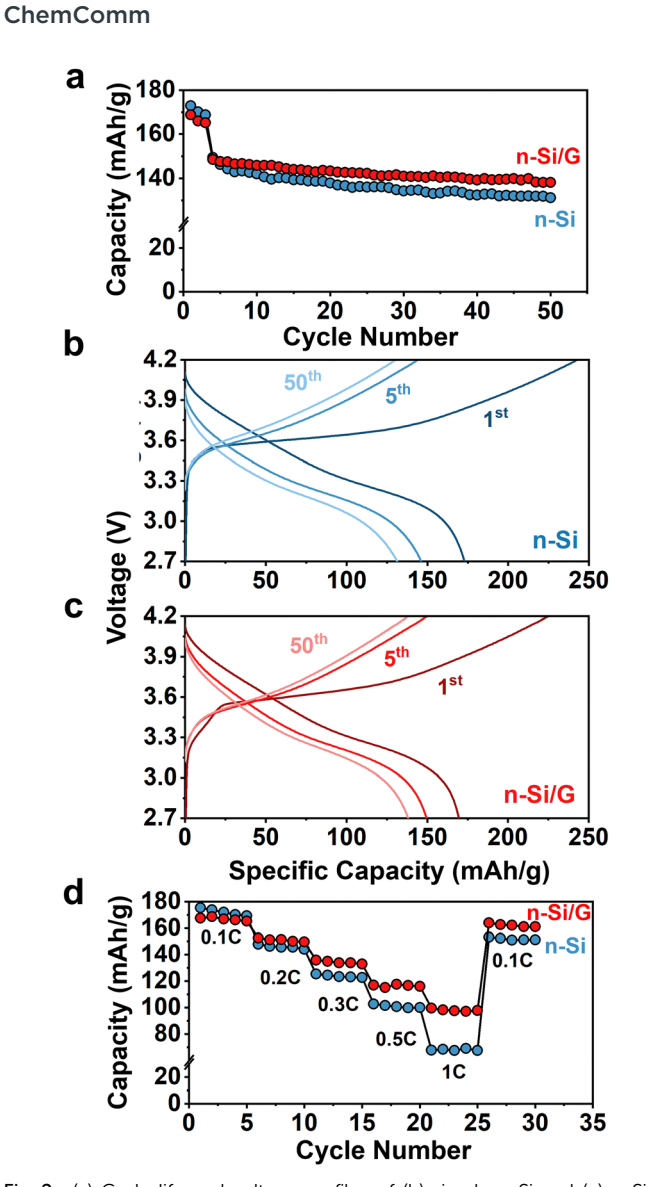


Fig. 2 (a) Cycle life and voltage profiles of (b) simple n-Si and (c) n-Si/G anodes in SSB full-cells paired with NMC622 cathodes. (d) Rate capability test of the full cells at RT, where both charging and discharging C-rates were varied from 0.1C to 1C.

mechanical contact resistance $(R_{\rm M})$ for P3 at the electrode/SE interface. The P4 peak group, which arises between 25 and 0.1 Hz, corresponds to the charge transfer resistance $(R_{\rm CT})$ from both the cathode and anode. Finally, the Warburg $(R_{\rm W})$ impedances observed in the Nyquist plots at f < 10 mHz correspond to the P5 peaks in the DRT profiles, which is attributed to solid-state Li⁺ diffusion.

Fig. 3d compares the individual contribution and evolution of resistance from different sources in the SSB full-cells over 50 cycles for the simple n-Si and n-Si/G anodes. Overall, all full-cells exhibited relatively larger $R_{\rm M}$ and $R_{\rm CT}$ components compared to other resistance contributions, indicating that the electrode/SE interface is the dominant source of cell resistance. After 50 cycles, the n-Si/G anode exhibited a lower total resistance increase of 24%, compared to 37% for the simple n-Si anode. Notably, the full-cell with the n-Si/G anode showed smaller increases of 18% in $R_{\rm M}$ and 52% in $R_{\rm CT}$, compared to 28% in $R_{\rm M}$ and 66% in $R_{\rm CT}$ for

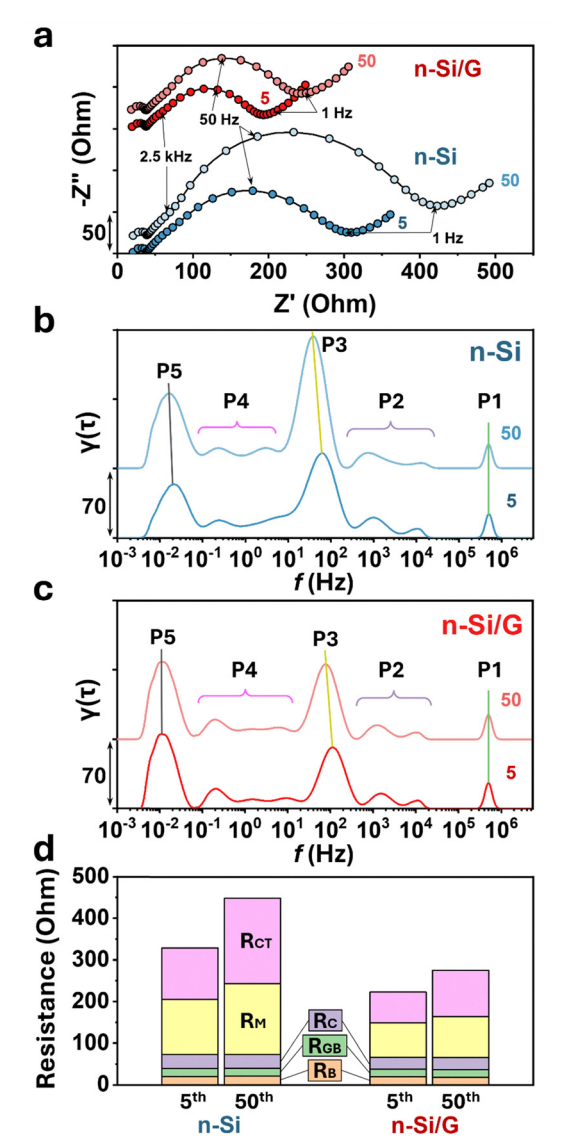


Fig. 3 (a) Nyquist plots (5th vs. 50th cycles) and corresponding DRT profiles of (b) simple n-Si and (c) n-Si/G anodes in SSB full-cells paired with NMC622 cathodes at 50% SOC and RT. (d) Individual contribution from different resistance sources in SSB full-cells and their evolution over 50 cycles, including bulk ($R_{\rm B}$), grain boundary ($R_{\rm GB}$), chemical contact ($R_{\rm C}$), mechanical contact ($R_{\rm M}$), and charge-transfer ($R_{\rm CT}$) resistances.

the simple n-Si anode. In contrast, the $R_{\rm B}$, $R_{\rm GB}$, and $R_{\rm C}$ values remained stable over 50 cycles. It is important to note that the SSB full-cells in this work employed an \sim 700 μ m thick SE layer, which negatively impacts the overall rate capabilities (Fig. 2d). However, the resistance contributions from the thick SE (*i.e.*, $R_{\rm B}$ + $R_{\rm GB}$) are substantially lower than other sources (*e.g.*, $R_{\rm M}$ and $R_{\rm CT}$), highlighting the superior interfacial stability between the n-Si/G anode and SE, relative to that of the simple n-Si anode.

The microstructures of the cycle-aged anodes in the SSB full-cells are shown in Fig. 4. After 50 cycles, the simple n-Si anodes exhibited large voids, up to 1 μ m in size, resulting from the substantial volumetric changes of the n-Si particles. These voids degrade the contact between the n-Si and SE, leading to an increase in $R_{\rm M}$, and subsequently hindering the charge-transfer reactions (*i.e.*,

Communication

a

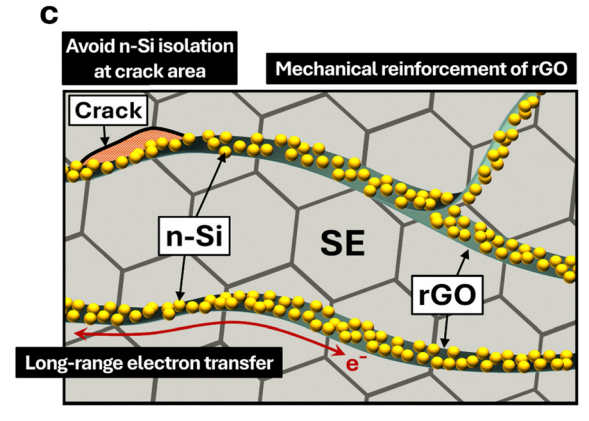


Fig. 4 FIB-SEM cross-sectional images of cycle-aged (a) simple n-Si and (b) n-Si/G anodes, recovered after 50 cycles. (c) Schematic illustration of the improvement mechanisms of n-Si/G anodes in SSB cells.

increase in $R_{\rm CT}$). In stark contrast, the cycle-aged n-Si/G anode showed voids with reduced scales compared to the simple n-Si anode. rGO and graphene have been widely incorporated into various ceramic matrices to improve the mechanical properties of ceramic/ rGO composites, such as fracture toughness, strength, and structural integrity. 18 In the n-Si/G composite anodes, rGO nanoplatelets serve as a flexible and robust mechanical scaffold, effectively accommodating the large volumetric changes of n-Si during cycling. This structural reinforcement suppresses interfacial degradation (e.g., large pore formation), thereby preserving the mechanical integrity of the n-Si/G anodes during cycling. Moreover, even in the presence of small cracks, the extended lateral size of the rGO (>1 µm) provides a continuous electron conduction network, preventing electrical isolation of the n-Si particles anchored onto the rGO.

In conclusion, this work demonstrates that the n-Si/G composite can serve as a promising anode material for SSB full-cells. Electrochemical and microscopy analyses suggest that the enhanced rate capability and cycle life, with a capacity retention of 93%, in full-cells with n-Si/G anodes can be attributed to robust interfacial contact between n-Si and rGO through Si-O-C bonding, mechanical reinforcement of the n-Si/G + SE composite structure, and stable long-range

electron transport facilitated by the rGO network. The EIS and DRT results suggest that resistance due to mechanical contact at the electrode/SE interface and charge transfer were the major components contributing towards the performance degradation. The improvement mechanism of the n-Si/G anodes is illustrated in Fig. 4c. Our results highlight the potential of n-Si/G as a promising anode material for high performance SSBs. Future research should aim to optimize the microstructure and electro-chemo-mechanical stability of the n-Si/G anodes, while also advancing scalable processing methods compatible with solid-state battery (SSB) manufacturing. In parallel, enabling stable operation under reduced external pressure could simplify cell design and lower system-level costs, thereby facilitating the broader commercialization of SSBs incorporating n-Si/G anodes.

Conflicts of interest

There are no conflicts to declare.

Data availability

The experimental methods for data collection are provided in the ESI.†

References

- 1 A. Morchhale, Z. Tang, C. Yu, R. Farahati and J.-H. Kim, Curr. Opin. Electrochem., 2023, 39, 101251.
- 2 D. H. S. Tan, Y.-T. Chen, H. Yang, W. Bao, B. Sreenarayanan, J.-M. Doux, W. Li, B. Lu, S.-Y. Ham, B. Sayahpour, J. Scharf, E. A. Wu, G. Deysher, H. E. Han, H. J. Hah, H. Jeong, J. B. Lee, Z. Chen and Y. S. Meng, Science, 2021, 373, 1494-1499.
- 3 J. Liu, K. Pan, H. Cho, M. Canova and J.-H. Kim, Electrochim. Acta, 2024, 500, 144746.
- 4 J. W. Yap, T. Wang, H. Cho and J.-H. Kim, Electrochim. Acta, 2023, 446, 142108.
- 5 M. Rana, Y. Rudel, P. Heuer, E. Schlautmann, C. Rosenbach, M. Y. Ali, H. Wiggers, A. Bielefeld and W. G. Zeier, ACS Energy Lett., 2023, 8, 3196-3203.
- 6 J. Liu, S. Y. Lee, J. Yoo, S. Kim, J.-H. Kim and H. Cho, ACS Mater. Lett., 2022, 4, 840-846.
- 7 J. Kim, C. Kim, I. Jang, J. Park, J. Kim, U. Paik and T. Song, J. Power Sources, 2021, 510, 230425.
- 8 J. K. Lee, K. B. Smith, C. M. Hayner and H. H. Kung, Chem. Commun., 2010, 46, 2025-2027.
- 9 M. Zhou, F. Pu, Z. Wang, T. Cai, H. Chen, H. Zhang and S. Guan, Phys. Chem. Chem. Phys., 2013, 15, 11394-11401.
- 10 K. Pan, F. Zou, M. Canova, Y. Zhu and J.-H. Kim, J. Power Sources, 2019, 413, 20-28.
- 11 Z. Liu, J. Lei, W. Liu, B. Fang, L. Xie, S. Dmytro and Q. Zhang, J. Eur. Ceram. Soc., 2023, 43, 4437-4442.
- 12 A. Kızılaslan, Ç. G. Türk, A. Miura and K. Tadanaga, Chem. Eng. J., 2024, **496**, 153588.
- 13 D. Zhang, P. Yu, Y. Zhang, X. Zhao and J. Yu, ACS Appl. Energy Mater., 2024, 7, 726-734.
- 14 T. H. Wan, M. Saccoccio, C. Chen and F. Ciucci, Electrochim. Acta, 2015, 184, 483-499.
- 15 C.-Y. Yu, J. Choi, J. Dunham, R. Ghahremani, K. Liu, P. Lindemann, Z. Garver, D. Barchiesi, R. Farahati and J.-H. Kim, J. Power Sources, 2024, 597, 234116.
- 16 T. Krauskopf, H. Hartmann, W. G. Zeier and J. Janek, ACS Appl. Mater. Interfaces, 2019, 11, 14463-14477.
- 17 P. Vadhva, J. Hu, M. J. Johnson, R. Stocker, M. Braglia, D. J. L. Brett and A. J. E. Rettie, ChemElectroChem, 2021, 8, 1930-1947.
- 18 V. B. Mohan, K. Lau, D. Hui and D. Bhattacharyya, Composites, Part B, 2018, 142, 200-220.